Carbon nanofiber bridged two-dimensional titanium carbide as a superior anode for lithium-ion batteries†

Zongyuan Lin,[a] Dongfei Sun,[a] Qing Huang,*[b] Jun Yang,[a] Michel W. Barsoum[c] and Xingbin Yan*[a]

MXenes, a novel family of two-dimensional metal carbides, are receiving intense attention for lithium-ion batteries (LIBs) and supercapacitors because they have high volumetric capacitance exceeding all carbon materials. However, serious interlayer stacking exists in MXene particles, which greatly decreases the electrical conductivity in the bulk and hinders the accessibility of interlayers to electrolyte ions. Thus, multi-stacked MXene particles exhibit low capacitance and poor rate capability. Herein, we report an effective strategy to directly improve the electrochemical performance of multi-stacked MXene ($Ti_3C_2T_x$) particles as LIB anode materials. It was successfully realized by growing conductive "carbon nanofiber (CNF) bridges" within the gaps of each $Ti_3C_2T_x$ particle as well as the outside. With the help of these CNFs, the as-prepared Ti_3C_2/CNF particles exhibited significantly improved reversible capacity compared with pure $Ti_3C_2T_x$ particles. More remarkably, even at an ultrahigh rate of 100 C, the capacity of Ti_3C_2/CNF hybrid particles was just slightly lower than that of pure $Ti_3C_2T_x$ particles at 1 C, and there was no capacity decay after 2900 cycles at 100 C, demonstrating excellent rate capability and superior long-term stability at the ultrahigh rate.

Introduction

MXenes, a new family of two-dimensional transition metal carbides,[1–4] have shown promise as electrode materials in electrochemical energy storage devices such as lithium-ion batteries (LIBs)[5–11] and supercapacitors with high volumetric capacitances exceeding all carbon materials.[12–15] When not delaminated, MXene particles with a multilayered microstructure are prepared by etching Al-containing MAX ceramic powders with concentrated acids (HF or HCl–LiF).[12,13,16,17] However, the removal of Al atoms and the termination of MXene surfaces by oxygen and fluorine-containing groups lead to inevitable layer-structure collapse/stacking among MXene layers during the subsequent drying process, resulting in a large decrease of the accessible surfaces and the formation of many nano- and submicron-scale spaces within each MXene particle.[1,12,18] The decreased accessibility of layer surfaces to electrolyte ions greatly hinders their full utilization, and these spaces may seriously decrease the electrical conductivity in the vertical-to-layer direction of individual MXenes.[19,20] Moreover, the irregular shapes and sizes of MXene particles lead to large contact resistance among them after the electrode manufacturing. Thus, stacked MXene particles exhibit relatively low capacitance and poor rate capability.

Delaminating the multilayer MXene particles and re-assembling them into a 'paper'-like structure is one strategy to improve their electrochemical performance.[6,12] If the 'paper' structure opens, then the electrolyte can access more active sites on the flakes and the resulting capacities can be enhanced. The electrochemical performance of paper-like electrodes can be further enhanced by adding interlayer spacers such as carbon nanotubes (CNTs) or polymers.[20,21] In the latter case, the CNTs and polymers are credited with improving the electrical conductivities of the electrodes and further increasing interlayer spaces for electrolyte ion access.[22,23]

Herein, we report, for the first time, on another effective strategy to improve the electrochemical performance of multilayer $Ti_3C_2T_x$ particles for use as LIB anode materials. We show that by growing conductive "carbon nanofiber" (CNF) bridges within the spaces of each MXene particle as well as between particles the Li capacity is enhanced. Such unique architecture can (1) provide numerous conductive CNF pathways within these voids/gaps to improve the electric transportation along the vertical-to-layer direction of each MXene, and (2) connect isolated MXene particles through CNFs to remarkably decrease

[a]Laboratory of Clean Energy Chemistry and Materials, State Key Laboratory of Solid Lubrication, Lanzhou Institute of Chemical Physics, Chinese of Academy of Sciences, Lanzhou, 730000, China. E-mail: xbyan@licp.cas.cn

[b]Division of Functional Materials and Nano-Devices, Ningbo Institute of Material Technology and Engineering, Chinese Academy of Science, Ningbo, 315201, China. E-mail: huangqing@nimte.ac.cn

[c]Department of Materials Science and Engineering, and A. J. Drexel Nanomaterials Institute, Drexel University, Philadelphia, PA 19104, USA

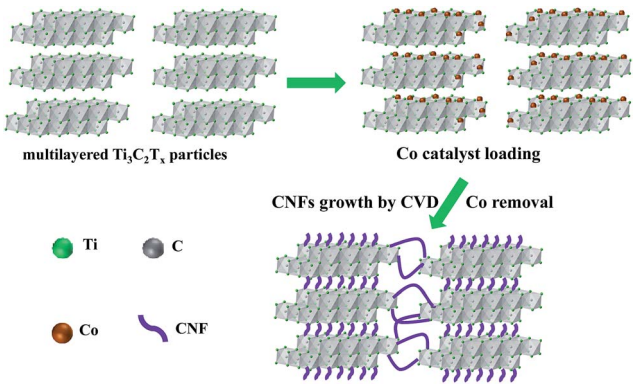

Fig. 1 Schematic showing the preparation of MXene/CNF hybrid particles.

their contact resistance. As a consequence, the as-prepared Ti_3C_2/CNF hybrid particles exhibited excellent electrochemical performance. A high reversible capacity of 320 mA h g^{-1} at 1 C was obtained for Ti_3C_2/CNF hybrid particles, which was nearly two times higher than that of pure $Ti_3C_2T_x$ particles. Even at a very high rate of 100 C, the capacity of Ti_3C_2/CNF hybrid particles at a steady state was just slightly lower than that of pure $Ti_3C_2T_x$ particles at 1 C, and there was no capacity decay after cycling 2900 times, demonstrating excellent rate capability and superior long-term stability at the ultrahigh rate.

In this study, $Ti_3C_2T_x$ was chosen as the starting MXene because its performance as a LIB anode is well studied.[6,8,11] A schematic of the procedure used to prepare $Ti_3C_2T_x$/CNF hybrid particles, using a simple chemical vapor deposition (CVD) technique, is shown in Fig. 1. First, a cobalt (Co) catalyst precursor, ($Co(NO_3)_2$) as well as poly(vinyl pyrrolidone) (PVP) were loaded inside and on the surface of multilayered $Ti_3C_2T_x$ particles by liquid-phase impregnation. The polymer was used to prevent the agglomeration of the catalyst particles.[24] The dried mixture was transferred into a horizontal quartz tube furnace for the growth of CNFs. Finally, Ti_3C_2/CNF hybrid materials were obtained by removing the Co catalyst. A series of precursor solutions with different PVP to Co salt mass ratios were used to control the growth of CNFs. According to their mass ratio (PVP to Co salt), the resulting Ti_3C_2/CNF hybrid samples were named Ti_3C_2–CNF-1-2, Ti_3C_2–CNF-1-5, Ti_3C_2–CNF-1-10, Ti_3C_2–CNF-1-15 and Ti_3C_2–CNF-1-20.

Results and discussion

The morphology and microstructure of multilayered $Ti_3C_2T_x$ particles and Ti_3C_2/CNF hybrid particles were investigated using a scanning electron microscope (SEM) and transmission electron microscope (TEM). As shown in Fig. 2a, the pristine $Ti_3C_2T_x$ particles were characterized by their typical accordion-like morphology, with many nano- and submicron-scale spaces between the flakes. And while these spaces provide important channels for ion intercalation/deintercalation, they decrease the electrical conductivity in the vertical-to-layer direction of individual $Ti_3C_2T_x$ particles, and thus hinder the practical application in LIBs.

Given that the as-synthesized $Ti_3C_2T_x$ multilayers are hydrophilic and have been shown to be excellent hosts for a number of cations,[12] it is reasonable to assume that upon reduction the impregnated Co salt, the Co would be uniformly attached to the surfaces of $Ti_3C_2T_x$ flakes and act as catalysts for the growth of the CNFs. As shown in Fig. 2b and S1,† after CVD growth, the resultant Ti_3C_2 particles (here the surface functional groups (–F and –OH) denoted as T in the starting $Ti_3C_2T_x$ MXene have been removed by the high-temperature treatment at 600 °C under an Ar/H_2 atmosphere (Fig. S2†)) were wrapped by a large number of vine-like CNFs. As importantly, the spaces between flakes in a single particle were also filled with many CNFs, forming CNF bridges between upper and lower flakes of individual Ti_3C_2 multilayered flakes (inset of Fig. 2b). Meanwhile, the open structure of the pristine multilayer particles was maintained, ensuring the facile access of electrolyte ions between the layers.

Fig. 2c shows a top view TEM image of a Ti_3C_2 particle from the Ti_3C_2–CNF-1-10 sample, in which a multitude of CNFs are seen extending between and around the different parts of the particle. The high-resolution TEM (HRTEM) image indicates that the Ti_3C_2 phase maintained its layered microstructure after the CVD process (Fig. 2d). The HRTEM image of a CNF is shown in Fig. 2e, and its diameter was about 20 nm. A pit generated by removing the Co catalyst was observed at the top of the CNF, suggesting that the growth of CNFs obeyed the tip growth mechanism. It should be noted that anatase TiO_2 nanoparticles with an average size of 20 nm were also observed on the surfaces of the Ti_3C_2 phase (Fig. 2f and S3†).

With the exception of anatase peaks in the CNF infused samples (see open crosses in Fig. 3a), when XRD diffraction patterns of the as-etched $Ti_3C_2T_x$ powders and those infused with CNFs are compared (Fig. 3a and S4†) they appeared unchanged. The survival of the MXene structure during CNF

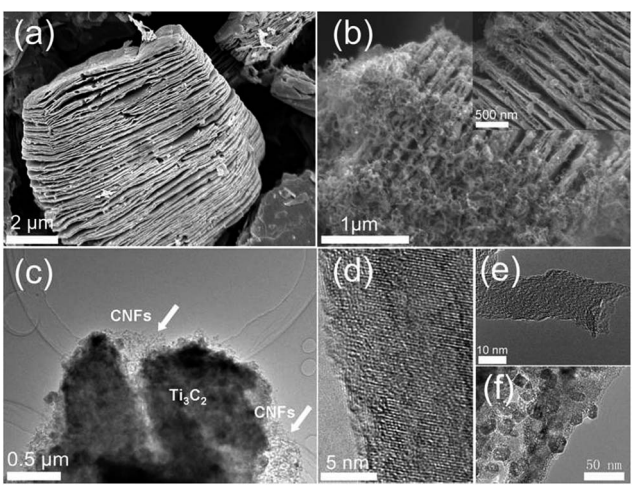

Fig. 2 Microstructure of $Ti_3C_2T_x$ and Ti_3C_2/CNF particles. (a) SEM images of the as-etched $Ti_3C_2T_x$ particles and (b) the Ti_3C_2–CNF-1-10 sample. The inset shows that some CNFs grow within the interlayer spaces of the Ti_3C_2 flakes. (c) TEM image of the Ti_3C_2–CNF-1-10 sample, (d) HRTEM images of a Ti_3C_2 flake and (e) a CNF in this sample, and (f) TEM image of TiO_2 particles on the Ti_3C_2 flake.

synthesis is crucial since it is the key unit for Li ion intercalation and de-intercalation. That is not to say that no changes occurred. After the CVD treatment, three anatase peaks (open crosses in Fig. 3a) were observed. The anatase is a result of the partial oxidation of the Ti_3C_2-flakes. The source of the oxygen is twofold: the O and OH terminations and the oxygen associated with the Co salt used in the CVD treatment. Indirect evidence for the latter is the fact that intensity ratios between the strongest anatase diffraction peaks and those of Ti_3C_2 increased with increasing Co salt content (Fig. S4†). Moreover, there were no diffraction peaks attributable to the CNFs most probably because of their amorphous, or nano-crystalline nature (Fig. 2e). This was also observed in some reported CNFs and carbon nanotubes grown by CVD.[25,26]

The C contents in all of the samples were measured using an elemental analyzer, as shown in Fig. S5.† Because the C content in the pure Ti_3C_2 sample after the same heat-treatment (at 600 °C under an Ar/H_2 atmosphere) was 13 wt%, the CNF contents in the Ti_3C_2–CNF samples can be calculated. As shown in Fig. S5,† the CNF content was 1.4 wt% for the Ti_3C_2–CNF-1-2 sample, 11.7 wt% for Ti_3C_2–CNF-1-5, 13.8 wt% for Ti_3C_2–CNF-1-10, 25.9 wt% for Ti_3C_2–CNF-1-15 and 20.0 wt% for Ti_3C_2–CNF-1-20. Among these the Ti_3C_2–CNF-1-15 sample showed the highest CNF content. The reason for this state of affairs could be due to the tendency of the Co catalyst particles to agglomerate at the highest loading. In this case, the catalytic activity of Co particles would decrease, resulting in the decrease of CNF content in the Ti_3C_2–CNF-1-20 sample.

The specific surface areas and pore structures of pure $Ti_3C_2T_x$ and Ti_3C_2–CNF-1-10 powders were analyzed by the Brunauer–Emmett–Teller (BET) method. Fig. 3b shows their nitrogen adsorption/desorption isotherms at 77 K. Both samples showed characteristics of meso- and macropores, but the Ti_3C_2–CNF-1-10 sample had a higher specific surface area of 20 $m^2\ g^{-1}$. Furthermore, as shown in Fig. 3c, the pore sizes of the pure $Ti_3C_2T_x$ sample were mainly distributed in the ranges of 16–50 nm, 50–74 nm and 117–159 nm. In comparison, an additional pore distribution in the range of 3–16 nm appeared for the Ti_3C_2–CNF-1-10 sample that could be attributed to new generated mesopores among CNFs.

To evaluate the influence of CNFs on multilayer Ti_3C_2 particles for LIB anode materials, about 10 μm thick electrodes (see Experimental and Fig. S6†) were produced, and cyclic voltammetry (CV), galvanostatic charge–discharge (GCD) cycling and electrochemical impedance spectroscopy (EIS) tests were carried out. As shown in Fig. S7,† there was a pair of reversible redox peaks at 1.7 and 2.1 V in the CV curves of the Ti_3C_2/CNF electrode at a scan rate of 0.2 mV s^{-1}, indicating the reversible process of lithiation and delithiation.[5,18,27] Fig. 4a shows the GCD curves of the Ti_3C_2–CNF-1-10 sample at a rate of 1 C (1 C = charge/discharge in 1 h, 320 mA h g^{-1}). Similar to other MXene materials,[3,5,6,11,27] there was no obvious plateau in the curves, meaning that the lithiation and delithiation took place over a large range of potentials. The initial discharge and charge capacities were 848 mA h g^{-1} and 407 mA h g^{-1}, respectively. The irreversible capacity loss was due to the formation of a solid electrolyte interphase (SEI) film at the electrode particles/electrolyte interface.[3,5,6,11,27] In the second cycle, the close values of discharge and charge capacity indicated the high reversibility. After this cycle, the decay in the reversible capacity was quite slight. For example, a reversible discharge capacity of 320 mA h g^{-1} was still maintained after 295 cycles, which is the same as the maximum predicted theoretical capacity of Ti_3C_2 monolayers (320 mA h g^{-1}) assuming a $Ti_3C_2Li_2$ stoichiometry.[8,10] In comparison, the pure $Ti_3C_2T_x$ electrode showed a reversible capacity of 112 mA h g^{-1} after 100 cycles (Fig. S8†), which was much lower than that of the Ti_3C_2–CNF-1-10 electrode. In our study, as shown in the cross-section SEM image of a working electrode (Fig. S6†), the thickness of the working electrode (having an active electrode material, a binder and a conductive additive) is about 10 μm. Thus, the volumetric capacity of the Ti_3C_2–CNF-1-10 sample is about 23 mA h cm^{-3}. We believe that the real value of the volumetric capacity could be higher without considering the binder and the conductive additive. As shown in Fig. S9,† the capacity of the $Ti_3C_2T_x$ particles after the heat-treatment was slightly higher than that of initial $Ti_3C_2T_x$ particles, indicating that the remarkable improvement in capacity in our system was due to the CNF growth instead of high-temperature CVD treatment. Moreover, as shown in Fig. S10,† the Ti_3C_2–CNF-1-10 electrode showed the highest capacity, indicating that the proper growth of CNFs is an effective method to enhance the capacity of multilayer $Ti_3C_2T_x$ particles. It may be due to the fact that a small number of CNFs cannot fully exert their function; however, too many CNFs will lower the electrochemical contribution from the original electro-active material. In fact, it is generally known that pure CNFs themselves, similar to CNTs, are not as good as Li anode materials.[28]

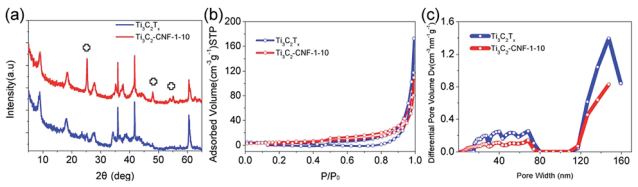

Fig. 3 Structure characteristics of the starting $Ti_3C_2T_x$ particles and Ti_3C_2/CNF hybrid particles (the Ti_3C_2–CNF-1-10 sample). (a) XRD patterns before (blue) and after the growth of CNFs. Patterns are shifted vertically for clarity. The crosses denote the locations of the anatase peaks. (b) N_2 sorption isotherms before (blue) and after the growth of CNFs. (c) The corresponding pore-size distributions.

The rate performance of the Ti_3C_2–CNF-1-10 electrode was investigated systematically. As shown in Fig. 4b, at rates of 1, 3.5, 8.5 and 30 C, the capacities of Ti_3C_2–CNF-1-10 were 320, 180, 145 and 106 mA h g^{-1}, respectively. When the rate was restored to 1 C, the capacity recovered to its initial value and maintained excellent stability at this rate. Fig. 4c compares the cycling stability of pure $Ti_3C_2T_x$ and Ti_3C_2–CNF-1-10 electrodes. The former electrode exhibited a steady-state capacity of 112 mA h g^{-1} at 1 C, which is very close to previously reported values.[6] In comparison, the Ti_3C_2–CNF-1-10 electrode showed a steady capacity of 320 mA h g^{-1} at the same rate, which was nearly two times higher than that of pure $Ti_3C_2T_x$. In order to further

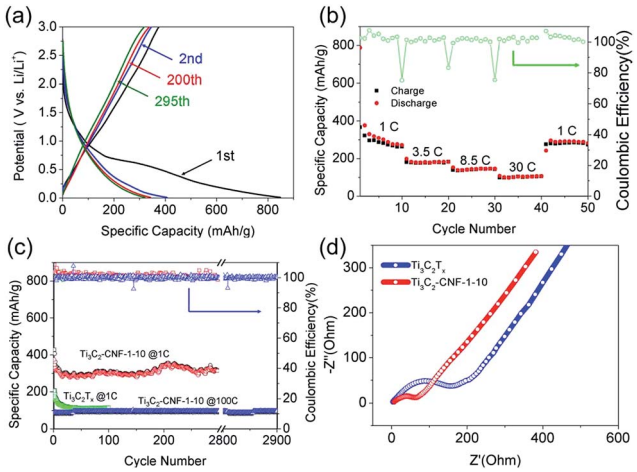

Fig. 4 (a) Charging/discharging curves of the Ti_3C_2–CNF-1-10 sample at 1 C. (b) Rate performance of the Ti_3C_2–CNF-1-10 sample. (c) Cycling stability of the $Ti_3C_2T_x$ sample at 1 C and the Ti_3C_2–CNF-1-10 sample at 1 C and 100 C. (d) EIS plots of the $Ti_3C_2T_x$ and Ti_3C_2–CNF-1-10 samples.

investigate the rate capability, the cyclic charge and discharge test of this Ti_3C_2–CNF-1-10 electrode was further run at an extremely high rate of 100 C. Even at that rate a steady-state capacity of 97 mA h g^{-1} was obtained which is slightly lower than that of the pure $Ti_3C_2T_x$ electrode at 1 C (Fig. 4c), demonstrating the excellent rate capability of this Ti_3C_2–CNF-1-10 electrode. More remarkably, even at the ultrahigh rate of 100 C, the Ti_3C_2–CNF-1-10 electrode was still able to provide the steady capacity of 97 mA h g^{-1} after 2900 cycles (Fig. 4c and S11†), indicating superior long-term cycling stability as well. As shown in the Fig. S12,† CNFs still remained in the Ti_3C_2 particles after the cycling test. The inset further shows that the CNFs did not undergo obvious structure change, indicating the existence of such 'conducting paths' even after the long-term cycling. These properties at a high rate are indicative of the fast diffusion of lithium ions in bulk, owing to the highly conductive and stable structure, and their short diffusion path lengths.

EIS measurements were carried out to further investigate the effect of CNFs on the charge transfer characteristics of the Ti_3C_2–CNF hybrid electrode, and Fig. 4d shows the Nyquist plots of $Ti_3C_2T_x$ and the Ti_3C_2–CNF-1-10 electrodes. Both impedance spectra consisted of a semicircle in the high to medium frequency region and an inclined line in the low frequency region. It is worth noting that the Ti_3C_2–CNF-1-10 electrode showed a much smaller semicircle diameter compared with the pure $Ti_3C_2T_x$ electrode, indicating much lower charge transfer impedance.

Therefore, these electrochemical results demonstrate that the appropriate introduction of CNFs effectively enhanced the electrical conductivity, and thus significantly improved the charge–discharge performance of Ti_3C_2–CNF hybrid particles. As shown in SEM and TEM images, such CNFs grown in the spaces of each stacked Ti_3C_2 particle formed conductive bridges between upper and lower Ti_3C_2 flakes. In this architecture, CNFs could provide effective conductive pathways to enable the fast interfacial electron transfer among Ti_3C_2 flakes. Simultaneously, CNFs also grew on the outside of each Ti_3C_2 particle, forming a 3D conductive network. These hair-like CNFs could serve as conductive bridges to connect Ti_3C_2 particles during the electrode manufacturing. With the help of these CNF bridges, the contact resistance among Ti_3C_2 particles could be greatly decreased, which benefits lithium insertion/extraction and the storage of lithium ions within the whole electrode, as exhibited in the Ti_3C_2/CNF hybrid particles with excellent electrochemical performances.

Conclusions

In conclusion, we have demonstrated a novel method to prepare Ti_3C_2/CNF hybrid particles as LIB anode materials. With the help of CNFs, the Ti_3C_2/CNF particles exhibited significantly higher reversible capacity and excellent rate performance compared with pure $Ti_3C_2T_x$ particles. A high reversible capacity of 320 mA h g^{-1} at 1 C was obtained, which was nearly two times higher than that of pure $Ti_3C_2T_x$ particles. Even at a very high rate of 100 C, the steady-state capacity of Ti_3C_2/CNF hybrid particles was just slight lower than that of pure $Ti_3C_2T_x$ particles at 1 C and showed superior long-term stability. In addition, such granular anode material might facilitate the practical industrial production of LIBs. Therefore, we believe that this is a breakthrough in MXene-based anode materials with high capacity and excellent rate capability and can significantly prompt the rapid development and applications of MXene materials in LIBs. Furthermore, we believe that the present synthetic strategy can be further extended to produce other MXene/CNF and MXene/CNT hybrid materials with impressive electrochemical performance for different electrochemical energy storage and generation devices.

Acknowledgements

This work was supported by the National Defense Basic Research Program of China (B1320133001) and the National Natural Science Foundation of China (91226202 and 21163010). Z. Y. Lin was supported by the Joint training master program associated with Prof. Lingbin Kong, School of Materials Science and Engineering, Lanzhou University of Technology.

Notes and references

1 M. Naguib, M. Kurtoglu, V. Presser, J. Lu, J. Niu, M. Heon, L. Hultman, Y. Gogotsi and M. W. Barsoum, *Adv. Mater.*, 2011, **23**, 4248.
2 M. Naguib, O. Mashtalir, J. Carle, V. Presser, J. Lu, L. Hultman, Y. Gogotsi and M. W. Barsoum, *ACS Nano*, 2012, **6**, 1322.
3 M. Naguib, J. Halim, J. Lu, L. Hultman, Y. Gogotsi and M. W. Barsoum, *J. Am. Chem. Soc.*, 2013, **135**, 15966.
4 M. Naguib, V. N. Mochalin, M. W. Barsoum and Y. Gogotsi, *Adv. Mater.*, 2014, **26**, 992.

5 M. Naguib, J. Come, B. Dyatkin, V. Presser, P. Taberna, P. Simon, M. W. Barsoum and Y. Gogotsi, *Electrochem. Commun.*, 2012, **16**, 61.

6 O. Mashtalir, M. Naguib, V. N. Mochalin, Y. Dall'Agnese, M. Heon, M. W. Barsoum and Y. Gogotsi, *Nat. Commun.*, 2013, **4**, 1716.

7 J. Hu, B. Xu, C. Ouyang, S. A. Yang and Y. Yao, *J. Phys. Chem. C*, 2014, **118**, 24274.

8 Q. Tang, Z. Zhou and P. Shen, *J. Am. Chem. Soc.*, 2012, **134**, 16909.

9 S. Zhao, W. Kang and J. Xue, *J. Phys. Chem. C*, 2014, **118**, 14983.

10 Y. Xie, M. Naguib, V. N. Mochalin, M. W. Barsoum, Y. Gogotsi, X. Yu, K. Nam, X. Yang, A. I. Kolesnikov and P. R. C. Kent, *J. Am. Chem. Soc.*, 2014, **136**, 6385.

11 D. Sun, M. Wang, Z. Li, G. Fan, L. Fan and A. Zhou, *Electrochem. Commun.*, 2014, **47**, 80.

12 M. R. Lukatskaya, O. Mashtalir, C. E. Ren, Y. D. Agnese, P. Rozier, P. L. Taberna, M. Naguib, P. Simon, M. W. Barsoum and Y. Gogotsi, *Science*, 2013, **341**, 1502.

13 M. Ghidiu, M. R. Lukatskaya, M. Zhao, Y. Gogotsi and M. W. Barsoum, *Nature*, 2014, **516**, 78.

14 Y. D. Agnese, M. R. Lukatskaya, K. M. Cook, P. Taberna, Y. Gogotsi and P. Simon, *Electrochem. Commun.*, 2014, **48**, 118.

15 M. D. Levi, M. R. Lukatskaya, S. Sigalov, M. Beidaghi, N. Shpigel, L. Daikhin, D. Aurbach, M. W. Barsoum and Y. Gogotsi, *Adv. Energy Mater.*, 2015, **5**, 1400815.

16 O. Mashtalir, M. Naguib, B. Dyatkin, Y. Gogotsi and M. W. Barsoum, *Mater. Chem. Phys.*, 2013, **139**, 147.

17 F. Chang, C. Li, J. Yang, H. Tang and M. Xue, *Mater. Lett.*, 2013, **109**, 295.

18 M. Naguib, O. Mashtalir, M. R. Lukatskaya, B. Dyatkin, C. Zhang, V. Presser, Y. Gogotsi and M. W. Barsoum, *Chem. Commun.*, 2014, **50**, 7420.

19 J. Halim, M. R. Lukatskaya, K. M. Cook, J. Lu, C. R. Smith, L. Näslund, S. J. May, L. Hultman, Y. Gogotsi, P. Eklund and M. W. Barsoum, *Chem. Mater.*, 2014, **26**, 2374.

20 Z. Ling, C. E. Ren, M. Zhao, J. Yang, J. M. Giammarco, J. Qiu, M. W. Barsoum and Y. Gogotsi, *Proc. Natl. Acad. Sci. U. S. A.*, 2014, **111**, 16676.

21 M. Zhao, C. E. Ren, Z. Ling, M. R. Lukatskaya, C. Zhang, K. L. Van Aken, M. W. Barsoum and Y. Gogotsi, *Adv. Mater.*, 2015, **27**, 339.

22 Z. Fan, J. Yan, T. Wei, G. Q. Ning, L. Zhi, J. C. Liu, D. X. Cao, G. L. Wang and F. Wei, *ACS Nano*, 2011, **5**, 2787.

23 S. H. Lee, V. Sridhar, J. H. Jung, K. Karthikeyan, Y. S. Lee, R. Mukherjee, N. Koratkar and I. K. Oh, *ACS Nano*, 2013, **7**, 4242.

24 W. Zhou, C. Rutherglen and P. J. Burke, *Nano Res.*, 2008, **1**, 158.

25 M. Zhao, Q. Zhang, X. Jia, J. Huang, Y. Zhang and F. Wei, *Adv. Funct. Mater.*, 2010, **20**, 677.

26 X. Jia, Y. Cheng, Y. Lu and F. Wei, *ACS Nano*, 2014, **8**, 9265.

27 J. Come, M. Naguib, P. Rozier, M. W. Barsoum, Y. Gogotsi, P.-L. Taberna, M. Morcrette and P. Simon, *J. Electrochem. Soc.*, 2013, **159**, A1368.

28 H. Zhang, Y. Zhang, X. Zhang, F. Li, C. Liu, J. Tan and H. M. Cheng, *Carbon*, 2006, **44**, 2778.